Eddy Current Imaging of Surface Breaking Defects by Using Monotonicity Based Methods

[1]G. Rubinacci, [2]A. Tamburrino and [2]S. Ventre

[1] Dipartimento di Ingegneria Elettrica, Università di Napoli "Federico II"
Via Claudio 21, Napoli, I-80125, Italy
rubinacci@unina.it

[2] DAEIMI, Università di Cassino
Via G. Di Biasio 43, Cassino (FR), I-03043
tamburrino@unicas.it, ventre@unicas.it

Abstract – This paper is in the framework of the non-destructive evaluation of conductive materials by means of eddy current testing. In particular, we consider the imaging of surface breaking volumetric defects. In this case, it is possible to use relatively "high-frequencies" and, in the limit of skin-depth negligible with respect to the relevant geometrical sizes and negligible displacement current, the problem can be modeled as a magnetostatic one. The elliptic nature of magnetostatic allows proving a monotonicity property of the operator mapping the defects geometry into the measured quantity. This makes possible to use a recently proposed fast (non-iterative) imaging algorithm.

***Keywords*:** Non-destructive testing, eddy current testing, inverse problem, and fast imaging algorithms.

I. INTRODUCTION

The solution of the inverse problem in a non destructive evaluation test based on eddy currents is usually formalized as the minimization of an error functional with respect to a given set of unknowns describing the features of the anomaly affecting the specimen under test. The evaluation of the error functional, relating the measurements to the computed data, requires the solution of the forward problem (compute the measurements for given anomalies) that should be repeated many times in the minimization procedure. Moreover the presence of local minima is a critical issue penalizing many local minimization algorithms. Recently a non-iterative method solving the inverse problem has been proposed for estimating a resistivity distribution approximated by a number of voxels [1-4]. The data consists of measurements of the impedance matrix at several frequencies acquired using a coil array. The method is based on a monotonicity property of the operator mapping the defects geometry into the measurements. However, in the approach adopted so far, the monotonicity has been achieved for the real part of the impedance matrix in the low frequency limit when the skin depth is larger than the relevant sizes of the problem. The evaluation of the impedance in this limit is a very difficult issue since the signal at low frequency is relatively weak and presence of noise can "destroy" the monotonicity property.

In this paper we prove the monotonicity property of the operator mapping the defects geometry into the measured quantity, in the high frequency limit. In this case the forward problem can be conveniently approximated by a magnetostatic equivalent model, thanks to the skin effect that imposes a vanishing field inside the specimen (and a vanishing normal component of the magnetic flux density on its surface). In this limit we can solve the inverse problem leading to the imaging of surface defects on a conductive specimen, in a non iterative way.

The paper is organized as follows: in Section 2 the mathematical model is described, in Section 3 the monotonicity is proved and in Section 4 numerical examples, aimed to verify the monotonicity and to show the performance of the inversion algorithm, are presented.

II. MATHEMATICAL MODEL

Let us consider a measurement system consisting of an array of several coils eventually mounted on a magnetic support that we assume to be linear (Fig. 1). The measured quantity is the impedance matrix (self and mutual impedances between coils) at the angular frequency ω. Under the assumption of negligible displacement current, the mathematical model is that of eddy current, eventually in the presence of magnetic materials. The mathematical model is, therefore,

$$\begin{cases} \nabla \times \mathbf{H} = \mathbf{J}_s \text{ in } \mathrm{IR}^3 \setminus V_c \\ \nabla \cdot (\mu \mathbf{H}) = 0 \text{ in } \mathrm{IR}^3 \setminus V_c \\ \nabla \times \mathbf{E} = -j\omega\mu \mathbf{H} \text{ in } V_c \\ \nabla \times \mathbf{H} = \sigma \mathbf{E} \text{ in } V_c \\ \nabla \cdot (\mu \mathbf{H}) = 0 \text{ in } V_c \end{cases} \quad (1)$$

together with proper continuity conditions on material interfaces and regularity conditions at infinity. In equation (1) V_c is the conducting domain, **E** and **H** are the electric and magnetic fields, respectively, σ is the electrical conductivity (**J**(**r**) = σ(**r**) **E**(**r**) in V_c, **J** is the induced current density), μ is the magnetic permeability (**B**(**r**) = μ(**r**) **H**(**r**) in IR^3, where **B** the magnetic flux density) and $\mathbf{J}_s$ is the prescribed source current density, that is the current density due to the currents circulating in the excitation coils. In addition, we assume the conductor to be non-magnetic.

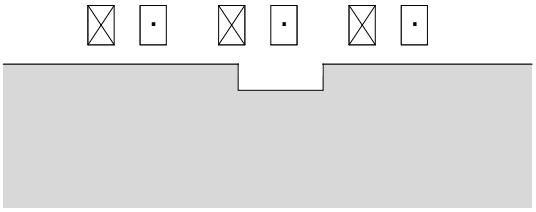

Fig. 1. A conductor is probed by an array of three coils. A surface breaking volumetric defect is present. The measured quantity is the impedance matrix (in this case a 3×3 symmetric matrix).

If the frequency is high enough so that the skin-depth is negligible with respect to the typical dimensions of the conductor, the fields vanish inside the conducting domain V_c. As long as the displacement current is negligible, the magnetic field outside the conductor satisfies a magnetostatic problem in the free space with the boundary condition $\mathbf{B} \cdot \hat{\mathbf{n}} = 0$ on ∂V_c,

$$\begin{cases} \nabla \times \mathbf{H} = \mathbf{J}_s \text{ in } \mathrm{IR}^3 \setminus V_c \\ \nabla \cdot \mathbf{B} = 0 \text{ in } \mathrm{IR}^3 \setminus V_c \\ \mathbf{B} \cdot \hat{\mathbf{n}} = 0 \text{ on } \partial V_c \\ \mathbf{B}(\mathbf{r}) = \mu(\mathbf{r}) \mathbf{H}(\mathbf{r}) \text{ in } \mathrm{IR}^3 \setminus V_c \end{cases} \quad (2)$$

Moreover, in this regime (negligible skin-depth and displacement current) the linked flux with the excitation coils approaches the linked flux for the magnetostatic problem of equation (2). Therefore, the impedance matrix approaches $j\omega \underline{\underline{L}}_{V_c}$, being $\underline{\underline{L}}_{V_c}$ the magnetostatic inductance matrix relating currents and linked fluxes in the excitation coils, $\underline{\varphi} = \underline{\underline{L}}_{V_c} \underline{i}$ where $\underline{\varphi}$ is the column vector of the linked fluxes and $\underline{i}$ is the column vector of the currents circulating in the coils. The mapping $V_c \subset \mathrm{IR}^3 \rightarrow \underline{\underline{L}}_{V_c}$ defines an operator hereafter termed Π.

III. MONOTONICITY

In this section we prove the following (monotonicity) property of the operator Π,

$$\Omega \subseteq \Xi \subset \mathrm{IR}^3 \Rightarrow \underline{\underline{L}}_{\Xi} \leq \underline{\underline{L}}_{\Omega} \quad (3)$$

where $\underline{\underline{L}}_{\Omega}$ ($\underline{\underline{L}}_{\Xi}$) is the (magnetostatic) inductance matrix following from equation (2) for V_c=Ω (V_c=Ξ) and $\underline{\underline{L}}_{\Xi} \leq \underline{\underline{L}}_{\Omega}$ means that the matrix $\underline{\underline{L}}_{\Xi} - \underline{\underline{L}}_{\Omega}$ is negative semi-definite. To prove equation (3), we first notice that the solution of equation (2) can be conveniently expressed in variational form (see [5] for instance) as,

$$\min_{\mathbf{a} \in A(V_c)} \Psi(\mathbf{a}') \quad (4)$$

where

$$\Psi(\mathbf{a}') = \frac{1}{2} \int_{\mathrm{IR}^3} \mu^{-1} |\nabla \times \mathbf{a}'|^2 \, \mathrm{d}V - \int_{\mathrm{IR}^3} \mathbf{J}_s \cdot \mathbf{a}' \, \mathrm{d}V \ , \quad (5)$$

$$A(V_c) = \left\{ \mathbf{a}' \in \mathrm{IL}^2_{\mathrm{rot}}(\mathrm{IR}^3) : \int_{V_c} |\nabla \times \mathbf{a}'|^2 \, \mathrm{d}V = 0 \right\}. \quad (6)$$

It is worth noting that if **a** is solution of equation (4), then

$$\Psi(\mathbf{a}) = -\frac{1}{2} \int_{\mathrm{IR}^3} \mu^{-1} |\nabla \times \mathbf{a}|^2 \, \mathrm{d}V \ , \quad (7)$$

and the inductance matrix $\underline{\underline{L}}_{V_c}$ can also be defined through the magnetostatic energy,

$$\frac{1}{2} \underline{i}^T \underline{\underline{L}}_{V_c} \underline{i} = \frac{1}{2} \int_{\mathrm{IR}^3} \mu^{-1} |\nabla \times \mathbf{a}|^2 \, \mathrm{d}V = -\Psi(\mathbf{a}). \quad (8)$$

The proof of equation (3) easily follows from the variational principle equation (4) and from $\Omega \subseteq \Xi \Rightarrow A(\Xi) \subseteq A(\Omega)$.

Let us assume that $\Omega \subseteq \Xi$, then $A(\Xi) \subseteq A(\Omega)$ and, therefore, from equation (4) it follows that $\Psi(\mathbf{a}_\Omega) \leq \Psi(\mathbf{a}_\Xi)$ where $\mathbf{a}_\Omega$ and $\mathbf{a}_\Xi$ are the solutions of equation (4) for V_c=Ω and V_c=Ξ, respectively. From equation (8) it follows,

$$-\frac{1}{2}\underline{i}^{T}\,\underline{\underline{L}}_{\Omega}\,\underline{i}=\Psi(\mathbf{a}_{\Omega})\le\Psi(\mathbf{a}_{\Xi})=-\frac{1}{2}\underline{i}^{T}\,\underline{\underline{L}}_{\Xi}\,\underline{i}\,, \qquad (9)$$

that, from the arbitrariness of the coils current vector $\underline{i}$, is equivalent to equation (3).

Monotonicity of equation (3) allows identifying volumetric anomalies by the fast and efficient imaging algorithm described in [1-4]. Here we sketch the main idea underlying the imaging algorithm. Let V be an unknown anomaly present in V_c and let V_k a test anomaly placed in a known position. If $V_k \subseteq V$ then $V_c \backslash V \subseteq V_c \backslash V_k$ and $\underline{\underline{L}}_{V_c \backslash V_k} \le \underline{\underline{L}}_{V_c \backslash V}$. Therefore, if $\underline{\underline{L}}_{V_c \backslash V_k} \le \underline{\underline{L}}_{V_c \backslash V}$ is false, then V_k is not contained in V. The test can be repeated for V_k taken in many different positions covering the "tentative region" where the anomaly is supposed to be present. In practice, $\underline{\underline{L}}_{V_c \backslash V}$ is a measured quantity whereas $\underline{\underline{L}}_{V_c \backslash V_k}$ is computed numerically.

IV. NUMERICAL EXAMPLES

IV.I Monotonicity: Numerical Validation

In this section we validate numerically monotonicity of equation (3) by means of simple canonical numerical examples. The test geometry consists of a conductive half-space (conductivity $5.88 \cdot 10^8$ S/m, copper) where several type of volumetric defects are considered. The numerical model consists of an edge-element based integral formulation where the unknown is the induced current density represented as the curl of the electric vector potential [6]. The height of the anomalies is 0.5mm, whereas their cross section is union of 0.33mm×0.33mm elements. The skin-depth can be retained negligible if significantly smaller than 0.5mm. For copper (conductivity $5.88 \cdot 10^8$ S/m) this is the case for frequencies greater than 172kHz (the skin-depth in copper at 172kHz is 0.05mm). It is worth noting that, in typical eddy current testing configurations, the displacement current is negligible up to few MHz, depending on the particular setting. From the numerical perspective, in these conditions, the unknown current density flows in a thin superficial layer mainly beneath the array of coils. Therefore, the finite element discretization has been limited to this superficial layer only (Fig. 2).

Figure 3 shows the different surface breaking test "anomalies" used to validate equation (3). Let V_c be the region (the half-space) occupied by the defect-free conductor and let V_1, V_2, V_3 and V_4 be the volumes occupied by the four different anomalies. To validate the monotonicity, we have carried out two different tests. In the first case we selected ordered pairs of anomalies (V_i, V_j) where the first anomaly V_i contains the second anomaly V_j (for instance, (V_1, V_2), (V_1, V_3) and (V_1, V_4)). Thus, from equation (3) we expect all eigenvalues of the difference $\underline{\underline{L}}_{V_c \backslash V_i} - \underline{\underline{L}}_{V_c \backslash V_j}$ to be positive. This is clearly the case as shown in Table 1 where is reported the sign index of $\underline{\underline{L}}_{V_c \backslash V_i} - \underline{\underline{L}}_{V_c \backslash V_j}$, defined as,

$$s\left(\underline{\underline{L}}_{V_c \backslash V_i} - \underline{\underline{L}}_{V_c \backslash V_j}\right) = \frac{\sum_k \lambda_k}{\sum_k |\lambda_k|} \qquad (10)$$

λ_k being the k-th eigenvalues of the matrix $\underline{\underline{L}}_{V_c \backslash V_i} - \underline{\underline{L}}_{V_c \backslash V_j}$, for different test cases. It is worth noting that the sign index is equal to +1 (−1) if $\underline{\underline{L}}_{V_c \backslash V_i} - \underline{\underline{L}}_{V_c \backslash V_j}$ is positive (negative) semi-definite and it assumes values in the open interval (−1, +1) when $\underline{\underline{L}}_{V_c \backslash V_i} - \underline{\underline{L}}_{V_c \backslash V_j}$ has eigenvalues with different sign.

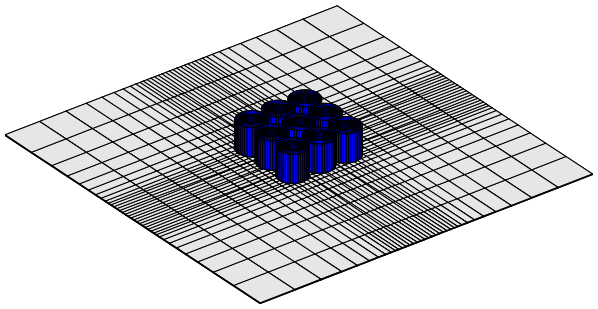

(a)

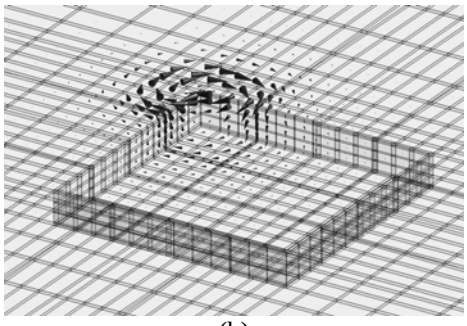

(b)

Fig. 2. (a) The finite element discretization together with the array made by 3×3 coils. The discretization is limited to a 0.05mm superficial layer. (b) The real (dominant) part of the induced eddy current density at 172kHz (skin-depth equal to 0.05mm) in the presence of a surface breaking volumetric anomaly. Only one coil is energized.

In the second test we have selected ordered pairs of anomalies (V_i, V_j) where V_i is not contained in V_j and vice versa (for instance (V_2, V_3), (V_2, V_4) and (V_3, V_4)). In this case (see Table 1) we are no longer guaranteed that

$\underline{\underline{L}}_{V_c \setminus V_i} - \underline{\underline{L}}_{V_c \setminus V_j}$ must be either a positive or negative semi-definite matrix.

Table 1. Sign index for different configurations. The element *ij* is the sign index for matrix $\underline{\underline{L}}_{V_c \setminus V_i} - \underline{\underline{L}}_{V_c \setminus V_j}$

	V_1	V_2	V_3	V_4
V_1	-	1	1	1
V_2	-1	-	0.861	0.879
V_3	-1	-0.861	-	0.426
V_4	-1	-0.879	-0.426	-

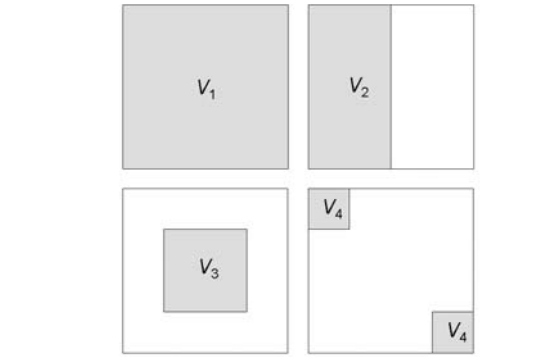

(a)

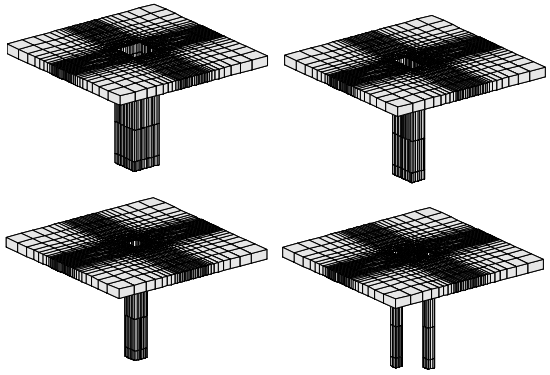

(b)

Fig. 3. (a) 2D (top) view of four different test anomalies having the same depth. (b) The corresponding 3D view (not in scale) consisting of only a thin superficial layer at the air-conductor interface (thickness 0.05mm right beneath the array of coils).

IV.II Monotonicity: Imaging Method

Here we apply the monotonicity to solve the inverse problem. The test configuration is similar to the one described in section 4.1. The region of interest is 36mm×36mm and it is subdivided into a 72×72 regular grid of test anomalies. From the computational viewpoint, each test anomaly is discretized using 2×2 elements in the transverse direction (see Fig. 4).

The probe is an array made by 23 coils arranged in the closest packed array configuration (see Fig. 4). Each coil has the inner radius of 0.3 mm, the outer radius of 0.6mm and the height of 6mm. The lift-off between the specimen and the probe is 2mm. In this test example we assume that each coil is made by one turn. The results can be easily scaled in case of coils made by an arbitrary number of turns.

To evaluate the visible region, i.e. the area "illuminated" by the probe, we computed the spatial distribution of the norm of $\underline{\underline{L}}_{V_c \setminus V_j} - \underline{\underline{L}}_{V_c}$ where the subscript *j* refers to the j^{th} test anomaly. Higher values of this norm are related to the visible region. From Fig. 4, it results that the visible region is made by 12×12 test anomalies, corresponding to a 6mm×6mm area. It is worth noting that the spatial map of the norm of $\underline{\underline{L}}_{V_c \setminus V_j} - \underline{\underline{L}}_{V_c}$ can be related to the order of magnitude of the maximum amount of measurement noise that does not "destroy" the reconstruction.

Since the scanned area (36mm×36mm) is larger than the visible region, the probe is placed at different locations. Specifically, the probe is moved onto a regular 8×8 grid corresponding to the intersections of the orthogonal lines in Fig. 5. The orthogonal lines subdivide the scanned area in 9×9 blocks; each block consists of 8×8 pixels (test anomalies). For a given pixel *j* (test anomaly *j*) in a block *B*, we compute the sign index,

$$s\left(\underline{\underline{L}}^{k}_{Meas} - \underline{\underline{L}}^{k}_{V_c \setminus V_j}\right) \tag{11}$$

related to the measurements when the probe is placed at the four corner of the block (k=1,..,4). In equation (11) $\underline{\underline{L}}^{k}_{Meas}$ and $\underline{\underline{L}}^{k}_{V_c \setminus V_j}$ are the (noisy) measured inductance matrix and the numerically computed inductance matrix related to pixel *j*, respectively (in both cases the probe is located in the k^{th} corner of the block *B*). Then, we associate to pixel *j* the quantity s_j that is the maximum of the four sign indices arising from the corners of block *B*.

In the absence of noise, when V_j is contained in the unknown anomaly *V*, we have s_j =1, as discussed in Sections 3 and 4.1 (lower values are obtained in the presence of noise). Finally, we compute the map $\hat{s}_j = 1/\left(1 - s_j\right)$. This last map provides a qualitative image of the defects (see Fig. 5) [1]. To obtain a quantitative reconstruction, we apply a threshold to the spatial map $\hat{s}_j$ (see Fig. 6). We found numerically that proper threshold values are those related to large gaps or local minima of the histogram of the values assumed by $\hat{s}_j$.

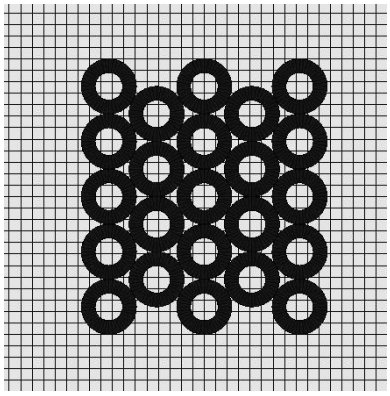

(a)

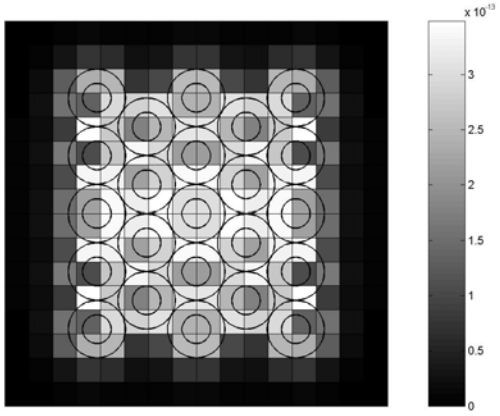

(b)

Fig. 4. (a) The array (view from the top) with a portion of the finite element mesh used during the computations. Each element has a transverse dimension of 0.25mm and each test anomaly consists of 2×2 elements in the transverse direction. (b) The array together with the spatial distribution of the norm of $\underline{\underline{L}}_{V_c \setminus V_j} - \underline{\underline{L}}_{V_c}$. The visible region is made by 12×12 pixels.

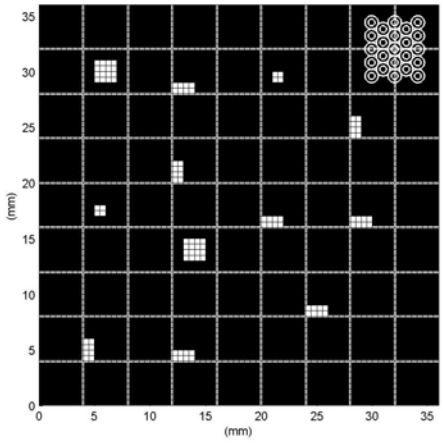

(a)

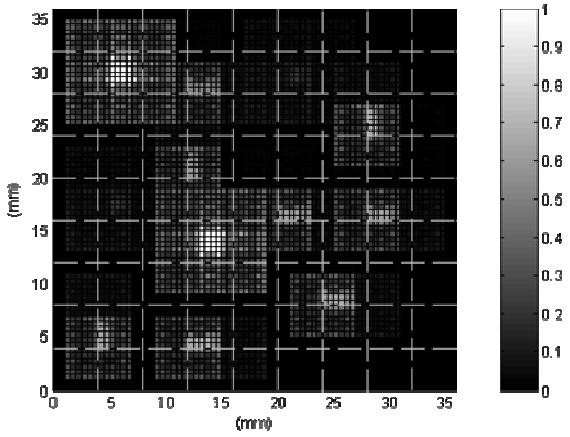

(b)

Fig. 5. (a) The distribution of the anomalies (white) together with the array and the grid use to place the array in different positions. (b) The (normalized) spatial maps of the $\hat{s}_j$'s.

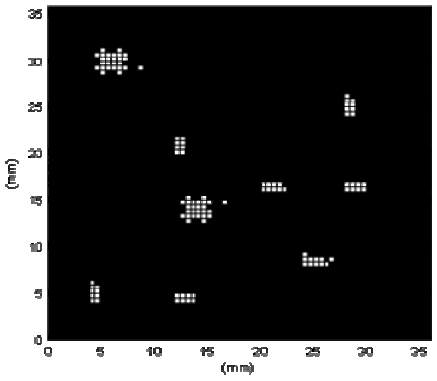

(a)

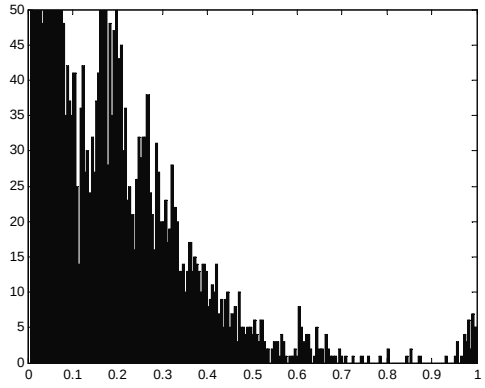

(b)

Fig. 6. (a) : the reconstructed map of anomalies obtained by applying a threshold of 0.54 to the spatial distribution of the $\hat{s}_j$'s. (b) : the histogram of the spatial distribution of the $\hat{s}_j$'s.

Finally, we mention that the measurements (matrices $\underline{\underline{L}}^k_{Meas}$) have been numerically computed and corrupted with an additive noise uniformly distributed in the range $(-\varepsilon,\varepsilon)$ where ε is 11% of the minimum norm of $\underline{\underline{L}}_{V_c \setminus V_j} - \underline{\underline{L}}_{V_c}$ in the visible region.

IV.III Noise and Resolution

Although this is beyond the scope of this work, in this subsection we present some considerations about noise and resolution in the framework of the proposed imaging method. The starting point is given by the following decomposition (see [3] for low frequency ECT) of $\underline{\underline{L}}^k_{Meas} - \underline{\underline{L}}^k_{V_c \setminus V_j}$,

$$\underline{\underline{L}}^k_{Meas} - \underline{\underline{L}}^k_{V_c \setminus V_j} = \left(\underline{\underline{L}}^k_{V_c \setminus \Omega} - \underline{\underline{L}}^k_{V_c}\right) + \left(\underline{\underline{L}}^k_{V_c} - \underline{\underline{L}}^k_{V_c \setminus V_j}\right) + \underline{\underline{N}}^k \quad (12)$$

where we have exploited that $\underline{\underline{L}}^k_{Meas} = \underline{\underline{L}}^k_{V_c \setminus \Omega} + \underline{\underline{N}}^k$, where Ω is the unknown anomaly, $\underline{\underline{L}}^k_{V_c \setminus \Omega}$ is the noise-free data and $\underline{\underline{N}}^k$ is the noise term. The amount of noise limits from below the minimum size of the V_j's, i.e. the resolution. Indeed, from equation (12) it follows that $\left\| \underline{\underline{L}}^k_{V_c} - \underline{\underline{L}}^k_{V_c \setminus V_j} \right\| \geq \alpha \left\| \underline{\underline{N}}^k \right\|$, where α is of the order of unity, is a necessary condition otherwise the noise term destroies the information content depending on V_j. Since the norm of $\underline{\underline{L}}^k_{V_c} - \underline{\underline{L}}^k_{V_c \setminus V_j}$ decreases as the size of V_j decreases, it is clear that the noise sets a limit to the achievable resolution or, vice versa, for a given resolution the maxim amount of noise compatible with the method is limited. Another limit to the resolution is set by the sensitivity of the instruments, specifically, $\left\| \underline{\underline{L}}^k_{V_c} - \underline{\underline{L}}^k_{V_c \setminus V_j} \right\| \geq \beta \left\| \underline{\underline{L}}^k_{V_c} \right\|$ where β is a dimensionless constant, significantly smaller than the unity, and representing the sensitivity of the measurement apparatus.

Figure 7 shows the behavior of $f = \max_k \left\| \underline{\underline{L}}^k_{V_c} - \underline{\underline{L}}^k_{V_c \setminus V_j} \right\|$ and $g = \max_k \left\| \underline{\underline{L}}^k_{V_c} - \underline{\underline{L}}^k_{V_c \setminus V_j} \right\| \Big/ \left\| \underline{\underline{L}}^k_{V_c} \right\|$ as a function of the of the ratio γ between the external radius of a coil and the diagonal of the voxel V_j. For the sake of simplicity the array is made by three coils (fig. 7(a)) and each coil consists of one single turn. The array is moved onto a regular 5×5 Cartesian grid with step-size of 0.5mm; the maximum in f and g is taken over these 25 different positions. It is interesting to see that increasing γ the function f decreases, i.e. the sensitivity with respect to the background measurement decreases. In other words, it increases the difficulty in appreciating the variations of the inductance matrix due to the test anomaly. We also notice that g presents a maximum for a proper value of γ. This means that for a given coil size, there is a proper value for the size of the voxel V_j that maximizes the immunity to the noise.

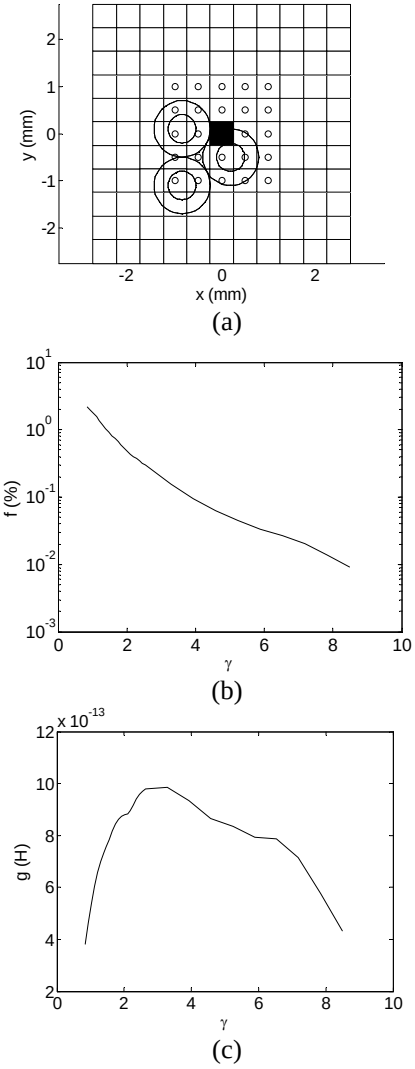

Fig. 7. (a) The voxel V_j (black pixel) together with the three coils probe of a given size, and the positions (o) where the probe is moved. (b) Plot of $f(\gamma)$. (c) Plot of $g(\gamma)$ assuming that the each coil has one single turn. γ is the ratio between the external radius of a coil and the diagonal of the voxel V_j.

V. CONCLUSIONS

The main contribution of this paper is the development of a fast imaging method based on the monotonicity property of the operator Π mapping the defects geometry into the inductance matrix measured at high enough frequencies. In this regime (negligible skin-depth and displacement current) the problem can be modeled as a magnetostatic one and this, thanks to the elliptic nature of magnetostatic, allows proving the monotonicity. Numerical examples confirm this property and, moreover, prove the effectiveness of the related fast imaging algorithm.

ACKNOWLEDGEMENTS

This work is supported in part by the Italian Ministry of University (MIUR) under a Program for the Development of Research of National Interest (PRIN grant # 2004095237) and by the CREATE Consortium.

REFERENCES

[1] A. Tamburrino and G. Rubinacci, "Fast methods for quantitative Eddy-current tomography of conductive materials," *IEEE Transactions on Magnetics*, MAG-42, no. 8, pp. 2017–2028, 2006.

[2] A. Tamburrino and G. Rubinacci, "A new non-iterative inversion method for electrical resistance tomography," *J. of Inverse and Ill-posed Problems*, vol. 18, pp. 1809-1829, December 2002.

[3] G. Rubinacci, A. Tamburrino, and S. Ventre, "Numerical optimization and regularization of a fast eddy current imaging method," *IEEE Transactions on Magnetics*, vol. 42, no. 4, pp. 1179-1182, 2006.

[4] A. Tamburrino, "Monotonicity based imaging methods for elliptic and parabolic inverse problems," *J. of Inverse and Ill-posed Problems*, vol. 14, no. 6, pp. 633-642, September 2006.

[5] A. Bossavit, *Computational Electromagnetism, Variational Formulations, Edge Elements, Complementarity*, Boston, MA: Academic Press, 1998.

[6] R. Albanese and G. Rubinacci, *Finite Element Methods for the Solution of 3D Eddy Current Problems, Advances in Imaging and Electron Physics*, edited by Peter W. Hawkes, vol. 102, pp. 1-86, Academic Press, 1998.

Guglielmo Rubinacci received the Laurea degree (*summa cum laude*) in Electronic Engineering from the University of Naples "Federico II," Naples, Italy, in 1975. Currently, he is a Full Professor of fundamentals in electrical engineering at the University of Naples "Federico II." He was the Dean of the Faculty of Engineering of the University of Cassino from 1996 to 2003. As a Fulbright-Hays Fellow he was a Visiting Scientist at MIT in 1980/81. He also engaged in research, in particular, at the Max Planck Institut fur Plasmaphysik, Garching and the Istituto Gas Ionizzati, CNR, Padova. He has been a Researcher at the Università di Napoli (1982/85), Professor in Charge and Associate Professor of electrical engineering at the Universities of Calabria (1979–84), Salerno (1984/88) and Napoli (1988/90), and Full Professor at the University of Cassino (1990–2004). He is the author/coauthor of more than 100 papers in refereed scientific journals and books and coeditor of two volumes. His research interests are mainly in computational electromagnetics with applications in several fields such as plasma engineering in tokamaks and electromagnetic nondestructive evaluation.

Antonello Tamburrino (M'97) received the Laurea degree (*summa cum laude*) in electronic engineering from the University of Naples "Federico II", Naples, Italy, in 1992, and the Ph.D. degree in electronic engineering from the Polytechnic of Turin, Turin, Italy, in 1996. Since December 2006, he is full professor of Electrotechnics at the College of Engineering, University of Cassino, Italy, where he is also the Head of the Laboratory of Computational Electromagnetism and Electromagnetic Nondestructive Evaluation. He has been Research Scientist (1994-2001) and Associate Professor (2001-2006) at the same university. From 2000 to 2002, he was a Visiting Scientist at Iowa State University, Ames. In 2002, he joined Michigan State University, East Lansing, where, since 2003, he has been an Adjunct Professor in the Department of Electrical and Computer Engineering. His research interests are mainly in the field of computational electromagnetics, with particular reference to electromagnetic non-destructive evaluation, inverse problems and integral methods. He is the coauthor of about 70 papers published in refereed scientific journals and books, among which several were invited papers. Dr. Tamburrino is member of the International Standing Committee of the Electromagnetic Nondestructive Evaluation Workshop, member of the Editorial Board of several international conferences and Reviewer for several journals.

Salvatore Ventre received in 1990 the Laurea Degree (*summa cum laude*) in Electrical Engineering from the University of Naples "Federico II", Italy. From 1993 he is at the Faculty of Engineering of the University of Cassino, Italy, where he is currently a Research Scientist. His research interests are mainly in computational electromagnetic with application in several fields such as electromagnetic nondestructive evaluation, electromagnetic compatibility, analysis of the time evolution of MHD equilibria, for the identification of the plasma boundary in tokamaks. He is author/coauthor of more than 30 technical papers on international journals and conference proceedings.